

OPEN ACCESS

Non-blind deconvolution with an alternating direction method of multipliers (ADMM) after noise reduction in nondestructive testing

To cite this article: W. Cheon *et al* 2019 *JINST* **14** P11032

View the [article online](#) for updates and enhancements.

You may also like

- [A novel lidar signal noise reduction algorithm based on improved deep belief network](#)
Shun Li, Jiandong Mao, Xin Gong et al.
- [Improving the sensitivity of Advanced LIGO using noise subtraction](#)
Derek Davis, Thomas Massinger, Andrew Lundgren et al.
- [Suppression of the low frequency intensity noise of a single-frequency Yb³⁺-doped phosphate fiber laser at 1083 nm](#)
Z Feng, C Li, S Xu et al.



ECS
The
Electrochemical
Society
Advancing solid state &
electrochemical science & technology

DISCOVER
how sustainability
intersects with
electrochemistry & solid
state science research

Non-blind deconvolution with an alternating direction method of multipliers (ADMM) after noise reduction in nondestructive testing

W. Cheon,^a B.J. Min,^b Y.S. Seo^b and H. Lee^c

^a*Department of Health Science and Technology, SAIHST, Sungkyunkwan University, Seoul 06351, South Korea*

^b*Department of Radiation Oncology, Chungbuk National University Hospital, Cheongju, 28644, South Korea*

^c*Department of Radiation Oncology, Gangnam Severance Hospital, Yonsei University College of Medicine, Seoul 06273, South Korea*

E-mail: bjmin@cbnuh.or.kr, holee@yuhs.ac

ABSTRACT: To ensure the quality of material, nondestructive testing is necessary, and radiography testing is the nondestructive technique most commonly used today. For inspection, the quality of a radiographic image is critical, and there are many image artifacts that can reduce inspection accuracies such as noise or blurring. The deterioration in spatial resolution caused by blur in both the X-ray imaging itself and the noise reduction process are particular problems. To tackle them, we implemented a non-blind deconvolution method that employs the alternating direction method of multipliers (ADMM) after noise reduction. Experimental results confirm that the proposed algorithm effectively restores edge sharpness. The 50% modulation transfer function of the restored image of a slit-camera was about 3.54 line-pairs per mm, which is about 2.5 times higher than that of the denoised image. Moreover, the edge preservation index values are about 0.82, 0.54, and 0.75 for the restored, denoised, and acquired images, respectively. Consequentially, the proposed method has the potential to increase inspection efficiency in industrial applications.

KEYWORDS: Inspection with x-rays; Data processing methods; Image filtering



Contents

1	Introduction	1
2	Materials and methods	2
2.1	Proposed restoration method	2
2.2	Experimental setup and materials	4
2.3	Evaluation of the image quality	5
3	Results and discussions	6
4	Conclusion	9

1 Introduction

Non-destructive testing is essential in industry to certify the quality of manufactured products, and radiography testing is a well-established non-destructive testing method; however, its use requires that workers be protected from radiation, and experienced workers are needed to interpret the results [1, 2]. Artifacts such as noise and blurring can reduce the test image quality, which must be kept high for the examination [3]. In particular, noise consists of noise correlated with X-rays (that is, Poisson noise) and noise uncorrelated with X-rays (mostly generated by electronic variation in the X-ray detector, in other words, Gaussian noise). Many studies have attempted to reduce noise in radiography [4]. However, existing noise reduction algorithms have an inherent problem: they blur the edges in the image [5]. Moreover, blur caused by the radiographic system further degrades the quality of the image.

Image deconvolution methods are widely used to restore blurred images. Non-blind deconvolution calculates the restored image using a point-spread function (PSF) that has been previously measured using image deconvolution. A variety of well-known non-blind deconvolution methods exist such as inverse filtering, Wiener filtering in the frequency domain, recursive Kalman filtering in the spatial domain, wavelet-based algorithm, and iterative methods [6–9]. Especially, the iterative method based on total variation (TV) [10, 11], total generalized variation (TGV) [12] and a penalty term (referred to as the “TGV-penalty” in this paper) is well known. However, the results often contain staircase artifacts and have a cartoon-like and unnatural appearance.

The goal of this paper is to propose a non-blind deconvolution approach that uses the alternating direction method of multipliers (ADMM) [13] to sharpen the image after the blurring caused by noise reduction. We also evaluate the ability of the proposed method to preserve radiographic image quality. From an X-ray imaging system, we acquired the original radiographic images of several test phantoms and determined the profile, line-spread function (LSF), and modulation transfer function (MTF) of the images processed by the proposed method. Moreover, the contrast-to-noise ratio (CNR) was measured to compare the image-quality performance of denoising algorithms and the

edge preservation index (EPI) was used to measure the degree of blurring as a quantitative index for both the original and deconvoluted images. The results show that the proposed method effectively increases the spatial resolution of radiographic images and has the potential to improve testing in an industrial setting.

2 Materials and methods

2.1 Proposed restoration method

Most image deconvolution methods are formulated as an inverse problem based on the standard image degradation model. The objective is to recover an artifact-free image f from the acquired (i.e., blurred and noisy) image I . Mathematically, a linear shift-invariant image degradation model is employed as follows [14, 15]:

$$I = f \otimes \otimes psf_{system} + n, \quad (2.1)$$

where the operator represents a 2D convolution operator, psf_{system} is a PSF that represents the rate of degradation in the system, and n is additive noise generated by the X-rays and imaging device. Recently, deep convolutional neural network approaches have achieved outstanding results in many image processing tasks such as noise reduction and inpainting [16]. Generally, a neural network is constructed as follows:

$$y = f_n(w_n f_{n-1}(\dots (w_3 f_2(w_2 f_1(w_1 x + b_1) + b_2) + b_3) \dots) + b_n), \quad (2.2)$$

where y is the output, x is the input, W_i is convolution matrix, b_i is a bias, and f_i is a nonlinear function. In this study, we used the denoising convolution neural network (DnCNN) architecture [17], which is based on a deep convolutional neural network created for noise suppression. This architecture consists of convolution layers (in our case, 3×3 convolutional filters), batch normalization, and the rectified linear unit (ReLU) activation function. The loss function is processed by means of back-propagation with adaptive moment estimation (ADAM). Details of the network's architecture and training conditions are given in table 1. The training set is composed of noise-free images and noise component images. To prepare a training set, the noise-free images were obtained with an high exposure that was about three times that of a conventional exposure image (i.e., the variation of noise in the noise-free images was approximately 0.1% in 14-bit pixel images, so is negligible) and the noise component images were generated using the *imnoise* function (i.e., we used Poisson parameters ranging from 0 to 1 and Gaussian parameters ranging from 1 to 30) in MATLAB (ver. 8.3, MathWorks, Natick, Massachusetts, U.S.A.) toolbox. We prepared 5,000 images for training and generated a total of 10.5 million image patches (i.e., the patch size was 64×64). Of the 5,000 images, 4,300 images were used for training, 300 images were used for validation, and the other images were used for testing to obtain the system accuracy. In this study, the mean value of the root-mean squared error between the label patch data and predicted patch data was about 5×10^{-3} .

The process of noise reduction results in the additionally blurred image g , expressed as follows:

$$g = f \otimes \otimes psf_{total}, \quad (2.3)$$

where psf_{total} is the total PSF that is added by the process of noise reduction. It is challenging to predict an accurate PSF for exact image restoration because eq. (2.3) is an ill-posed problem. We measured psf_{total} using a slit camera and image deconvolution.

Table 1. Denoising convolution neural network architecture and hyper-parameters.

Hyperparameters	Dimension
Patch size	64×64
Layers	Convolution and rectified linear unit (ReLU) (1 st) Convolution, batch normalization, and ReLU (2 nd to 14 th) Convolution (15 th)
Number of filters	64
Size of filters	3×3
Epoch	50
Learning rate	10^{-1} to 10^{-4}
Loss function	Adaptive momentum estimation
Output data	Residual data

In this study, we propose an ADMM-based non-blind deconvolution algorithm based on a differential weighted l^1 -norm regularization penalty term, which is a second-order term. In this algorithm, we solve the core optimization problem by minimizing objective function $\Phi(f^{(k)})$, which is the solution to the following convex optimization problem f^* :

$$f^* = \arg \min_{f^{(k)} \in Q} \left(\frac{u}{2} \|f^{(k)} \otimes \otimes ps f_{\text{total}} - g\|_2^2 + \|\nabla f^{(k)}\|_1 \right), \quad (2.4)$$

where $\frac{u}{2} \|f^{(k)} \otimes \otimes ps f_{\text{total}} - g\|_2^2$ is the fidelity term, $\|\nabla f^{(k)}\|_2$ is the differential weighted l^1 -norm regularization term, and u is a weighting parameter (in this study, we used $u = 10,000$). The convex optimization problem described in eq. (2.4) can be solved stably but efficiently using the intermediate variable r for the fidelity term as follows:

$$\begin{aligned} f^* &= \arg \min_{f^{(k)} \in Q} \varphi \left(\frac{u}{2} \|f^{(k)} \otimes \otimes ps f_{\text{total}} - g\|_2^2 + \|r\|_1 \right), \\ r &= \nabla f^{(k)}, \end{aligned} \quad (2.5)$$

Then, the augmented Lagrangian of eq. (2.5) can be described as follows:

$$L(f^{(k)}, r, y) = \frac{u}{2} \|f^{(k)} \otimes \otimes ps f_{\text{total}} - g\|_2^2 + \|r\|_1 - y(r - \nabla f^{(k)}) + \frac{\rho}{2} \|r - \nabla f^{(k)}\|_2^2, \quad (2.6)$$

where y is the Lagrange multiplier of constraint $r = \nabla f^{(k)}$ in the row and column directions and ρ is a regularization parameter of quadratic penalty term $\|r - \nabla f^{(k)}\|_1$. The goal of the augmented Lagrangian method is to find an optimized solution at a saddle point of $L(f^{(k)}, r, y)$. Therefore, we

use the ADMM, which splits eq. (2.6) into the following three sub-problems:

$$f^{(k+1)} = \arg \min_{f^{(k)} \in Q} \|f^{(k)} \otimes \otimes ps f_{\text{total}} - g\|_2^2 - y^{(k)}(r^{(k)} - \nabla f^{(k)}) + \frac{\rho}{2} \|r^{(k)} - \nabla f^{(k)}\|_1, \quad (2.7)$$

$$r^{(k+1)} = \arg \min_{r^{(k)} \in Q} \|r^{(k)}\|_1 - y^{(k)}(r^{(k)} - \nabla f^{(k+1)}) + \frac{\rho}{2} \|r^{(k)} - \nabla f^{(k+1)}\|_2^2, \quad (2.8)$$

$$y^{(k+1)} = y^{(k)} - \rho(r^{(k+1)} - \nabla f^{(k+1)}). \quad (2.9)$$

Here, eq. (2.8) updates $f^{(k+1)}$ using g , and the next gradient image $r^{(k+1)}$ is calculated using the updated $f^{(k+1)}$ in eq. (2.9). Lagrange multiplier $y^{(k+1)}$ is also updated in eq. (2.10). The final image f^* is obtained using an iterative loop. Details of the augmented Lagrangian problem can be found in [16].

Figure 1 shows a simplified view of the whole schematic diagram of the X-ray image restoration considering the noise and blur prediction. First, we implemented the noise prediction using DnCNN architecture for noise subtraction and then we performed the blur measurement using the slit camera to obtain the restored image.

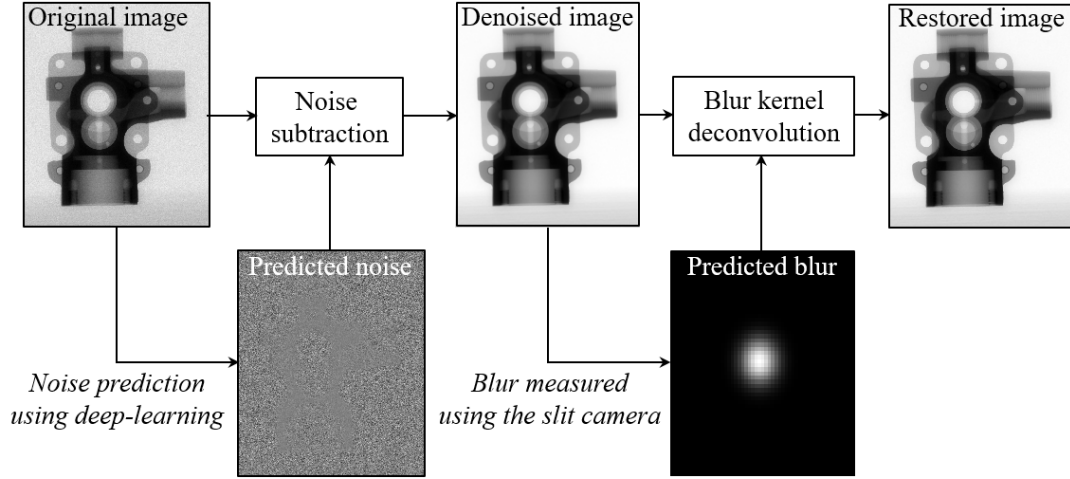


Figure 1. Proposed X-ray image restoration method including noise and blur prediction.

2.2 Experimental setup and materials

Figure 2 shows a schematic illustration of the experimental setup. An X-ray tube (MXR Corp., 30- μm focal spot) was operated at 70 kVp and 10 mAs to acquire the image. The detector has a resolution of $1,200 \times 1,200$ pixels with a 50- μm pixel size. The mechanical system was designed with a source-to-detector distance of 400 mm. Here, the lead-beam limiter was located in front of the X-ray tube for beam forming and was 1.0 mm in size.

Figure 3 shows the test materials: (a) a slit camera (Nuclear Associate Corp., 07-624-1) with a slit width of 10 μm to measure the LSF and the MTF, (b) a die-cast air pump, and (c) a line chart phantom (Nuclear Associates, 07-553), which consists of a 50- μm thick lead test pattern encased in plastic. Table 2 presents the line pairs per mm (lp/mm) value for each resolution in the line chart phantom.

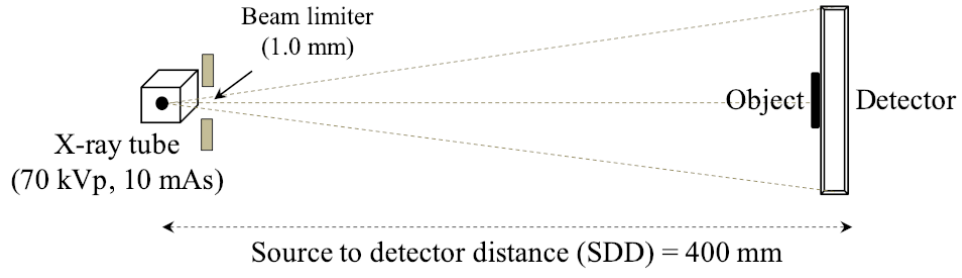


Figure 2. Simplified model of the radiographic imaging system experimental setup.

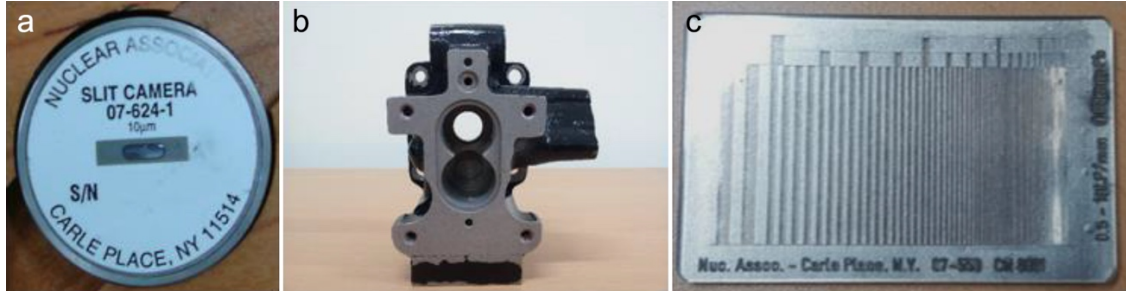


Figure 3. Test materials: (a) slit camera, (b) air pump, and (c) line chart phantom.

Table 2. Line pairs per mm for each resolution in the line chart phantom.

Group	lp/mm	Group	lp/mm
1	0.25	12	2.9
2	0.5	13	3.5
3	0.6	14	4.2
4	0.7	15	5.0
5	0.85	16	6
6	1.0	17	7
7	1.2	18	8.5
8	1.4	19	10
9	1.7	20	8.5
10	2.0	21	7
11	2.4	22	6

2.3 Evaluation of the image quality

In this study, we measured the profile, LSF, MTF, CNR, and EPI of images to determine their quality. The LSF is obtained using the oversampling method to ensure the accuracy of the profile [18]. The MTF is the magnitude of the response over spatial frequencies when information is transferred through an imaging device. Theoretically, the MTF can be defined as follows:

$$\text{MTF}(u) = |\mathfrak{F}\{\text{LSF}(y)\}|, \quad (2.10)$$

where y is the image domain position, u is the frequency domain position, and \mathfrak{F} is the Fourier transform operator. Here, MFT values closer to 1 indicate a higher information transfer rate over spatial frequencies in the imaging system [19].

The CNR was defined according to the following formula:

$$\text{CNR} = \frac{|G_{\text{ROI}_1} - G_{\text{ROI}_2}|}{\sqrt{S_{\text{ROI}_1}^2 + S_{\text{ROI}_2}^2}} \quad (2.11)$$

where G_{ROI} and S_{ROI} are respectively the mean value and standard deviation in the selected ROI_1 and ROI_2 .

The EPI of image p_2 is given by the following equation:

$$\text{EPI} = \frac{\Gamma(\Delta p_1 - \overline{\Delta p_1}, \Delta p_2 - \overline{\Delta p_2})}{\sqrt{\Gamma(\Delta p_1 - \overline{\Delta p_1}, \Delta p_1 - \overline{\Delta p_1})} \cdot \sqrt{\Gamma(\Delta p_2 - \overline{\Delta p_2}, \Delta p_2 - \overline{\Delta p_2})}}, \quad (2.12)$$

where

$$\Gamma(a, b) = \sum_{i,j \in \text{ROI}} a(i, j) \cdot b(i, j), \quad (2.13)$$

Here, $\overline{\Delta p}$ is the mean of image p filtered by a 3×3 Laplacian filter, and p_1 is the reference image of p_2 . The EPI is an index for evaluating the edge preservation in an image and has a range of 0 to 1. EPI values closer to 1 indicate a sharper edge structure in the image. More details of the EPI can be found in [20].

3 Results and discussions

Figure 4 shows images obtained by the proposed method using the slit camera, which is used for measuring the psf_{total} of the system. Figure 5 shows the LSFs of the profiles for line A in figure 4. Figures 5(a)–(c) show the results for the original image, denoised image, and restored image, respectively. In the LSFs, we observe a change in the blur after noise reduction and the image is deconvolved using psf_{total} . The sigma of the original image LSF is 0.9104 pixels. Moreover, the sigma of the denoised image LSF is almost twice that of the original image, indicating image blurring. Finally, the sigma of the restored image LSF is smaller than those of the other two images. Figure 6 shows the MTFs derived from the measured LSFs shown in figure 5. The spatial frequency of all of LSFs measured at 50% MTF were about 3.12 lp/mm (original image), 1.44 lp/mm (denoised image), and 3.54 lp/mm (restored image). These results evidence that the proposed algorithm improves the sharpness of the image. In addition, they indicate that the blur caused by the noise reduction algorithm and the inherent blur of the X-ray imaging system are corrected by the proposed algorithm. The LSF of the denoised slit image was used as the psf_{total} in the subsequent experiments.

Figure 7 shows the results for the original image (left), denoised image (middle), and restored image (right) of the air pump, and figure 8 shows the magnified results of boxes A and B in figure 7. The image restored using the proposed algorithm has better preserved fine image details than the other images. In particular, the sharpness of the spring in the restored image is better than in

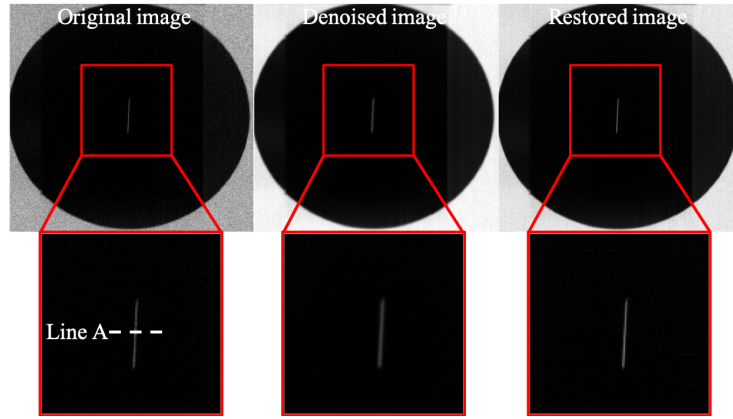


Figure 4. Slit camera images processed using the proposed method.

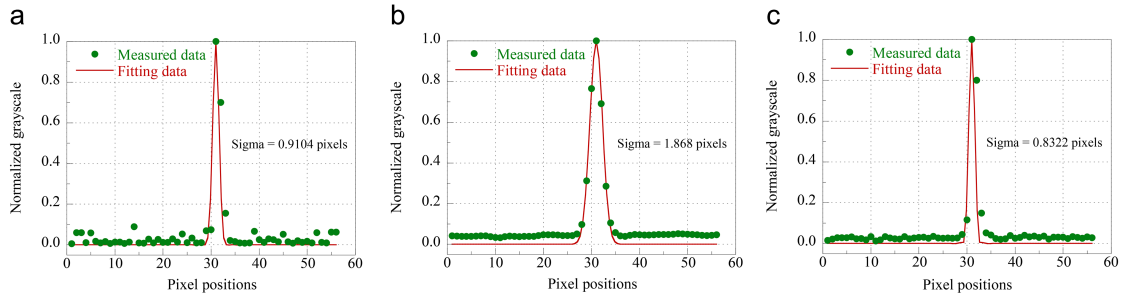


Figure 5. Line spread functions of the images in figure 4: (a) original image, (b) denoised image, and (c) restored image.

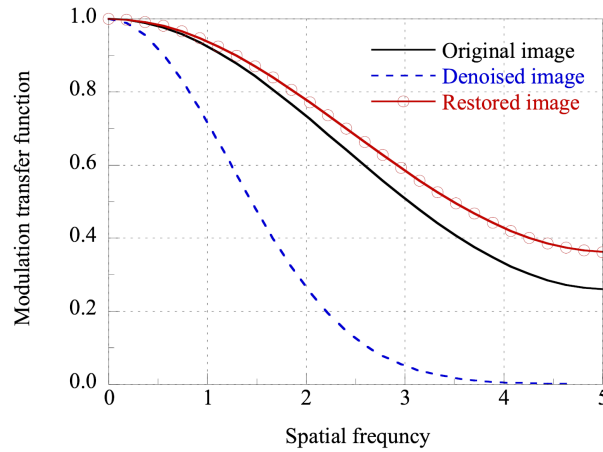


Figure 6. Modulation transfer functions derived from the line spread functions in figure 5.

the denoised image. In addition, noise is rarely amplified in the restored image, even though the deconvolution process with the predicted PSF is a kind of high pass filtering. The EPI values of the images are about 0.82, 0.54, and 0.75 for the restored, denoised, and original images, respectively. Therefore, this result indicates that the proposed algorithm is able to restore blurred images.

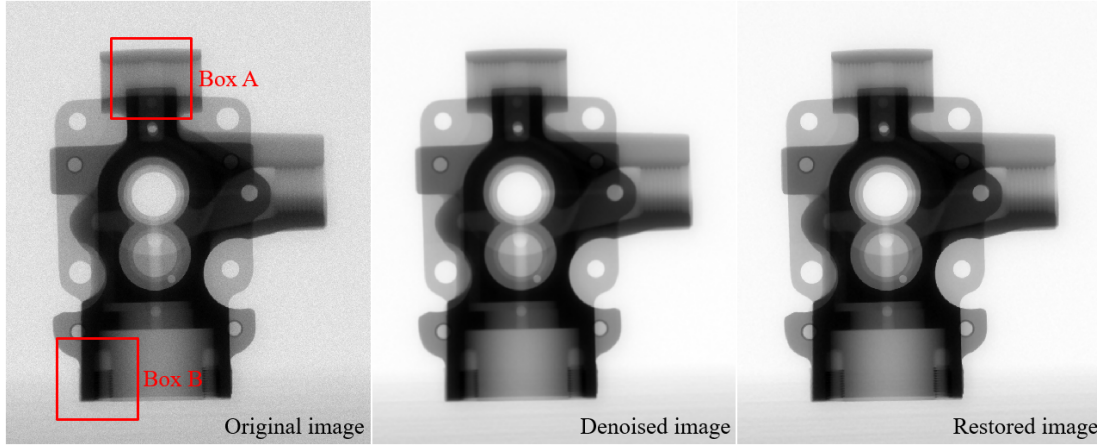


Figure 7. Air pump images processed using the proposed method: original image (left), denoised image (middle), and restored image (right) using the air pump.

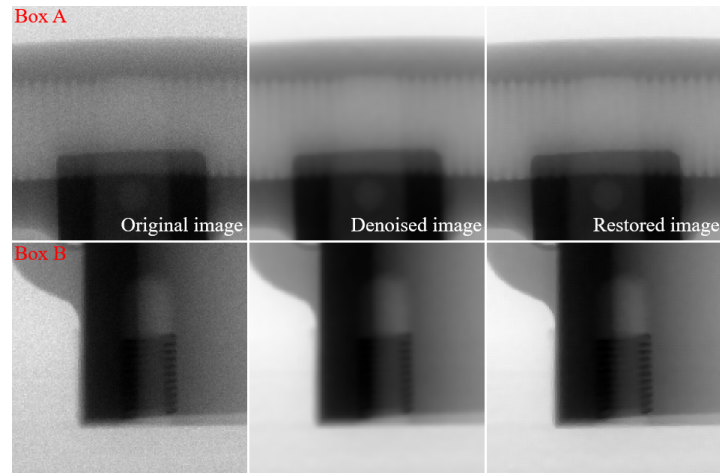


Figure 8. Magnified images of the original (left), denoised (middle), and restored (right) images in Boxes A and B in figure 7.

The images of the line chart phantom are used to compare the edge preservation of the proposed method with that of another algorithm. Figure 9(a) shows the original image (top left) as well as the denoised images obtained by the median filter (top right), the Wiener filter (bottom left), and DnCNN (bottom right). The median filter and Wiener filter used 5×5 masks. For the quantitative evaluations, we measured the CNR values indicated by box A in figure 9(b). The CNR value of the image processed by DnCNN was about three times higher than those of the denoised images using the median filter and Wiener filter, which were about 10.85. Figure 10(a) shows the images processed using DnCNN (top left), unsharp mask (top right), TGV-penalty (bottom left), and the proposed method (bottom right). The enlarged areas indicated by box A are shown in figure 10(b). In addition, figure 11 shows the profiles of line A of figure 10(b), which ranges from group 6 to group 22. In contrast to other profiles, the profile of the image restored by the proposed method enables groups 15 to 17 to be distinguished.

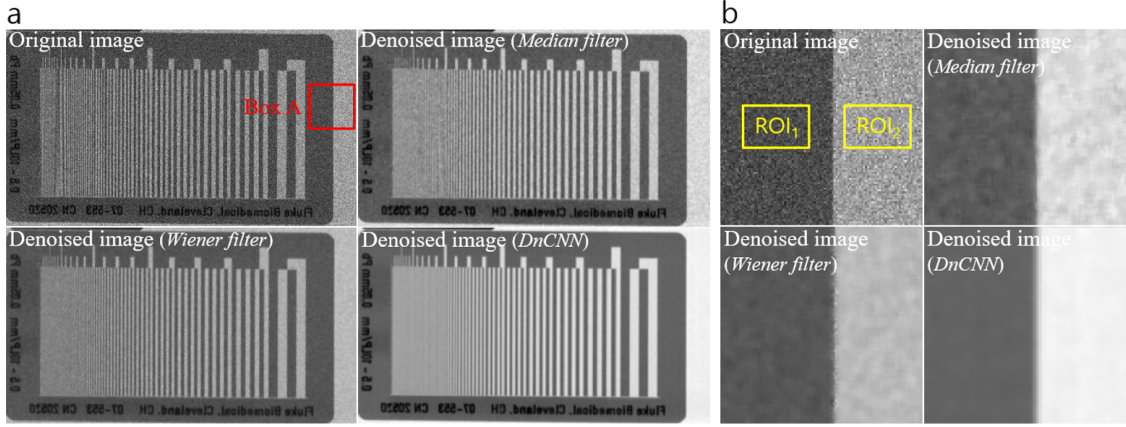


Figure 9. Line chart phantom images processed using the proposed method: (a) Original image (top left), denoised image (median filter: top right), denoised image (Wiener filter: bottom left), and denoised image (Denoising convolution neural network (DnCNN): bottom right). (b) Magnified views of the images in Box A.

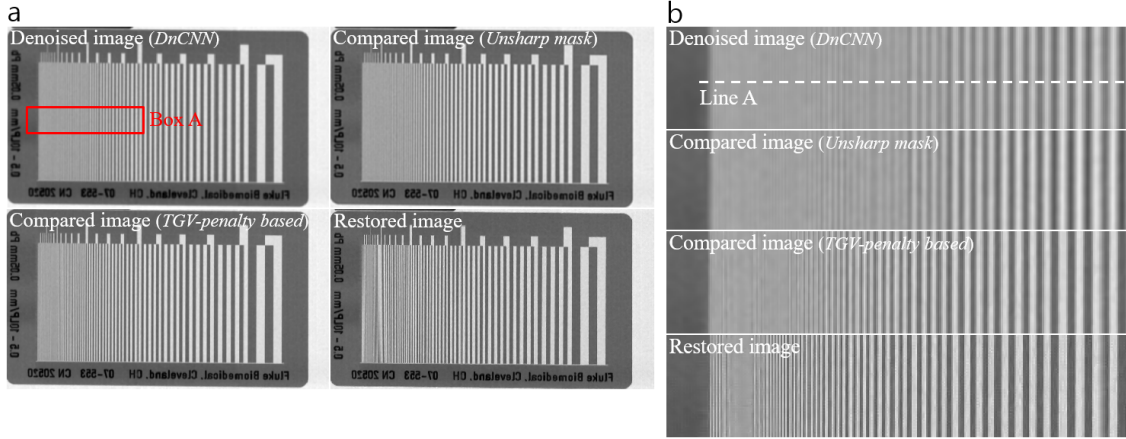


Figure 10. Line chart phantom images processed using the proposed method: (a) Denoised image (Denoising convolution neural network (DnCNN): top left), comparison image (unsharp mask: top right), comparison image (total generalized variation-penalty based method (TGV-penalty): bottom left), and image restored using the proposed method (bottom right). (b) Magnified views of the images in Box A.

4 Conclusion

In this paper, we introduced an ADMM-based blind deconvolution method to improve the spatial resolution in radiographic images. The proposed method consists of blur kernel estimation and non-blind deconvolution. We demonstrated that the proposed method effectively reduced the total blur, which consists of blurring caused by noise reduction and blurring inherent to the X-ray system. In an experiment using the slit camera, the 50% MTF of the restored image is about 3.54 lp/mm, which is about 2.5 times higher than that of the denoised image. Moreover, the EPI of the restored image is about 1.5 times higher than that of the denoised image. We believe that the proposed method has the potential to increase inspection efficiency in the industry.

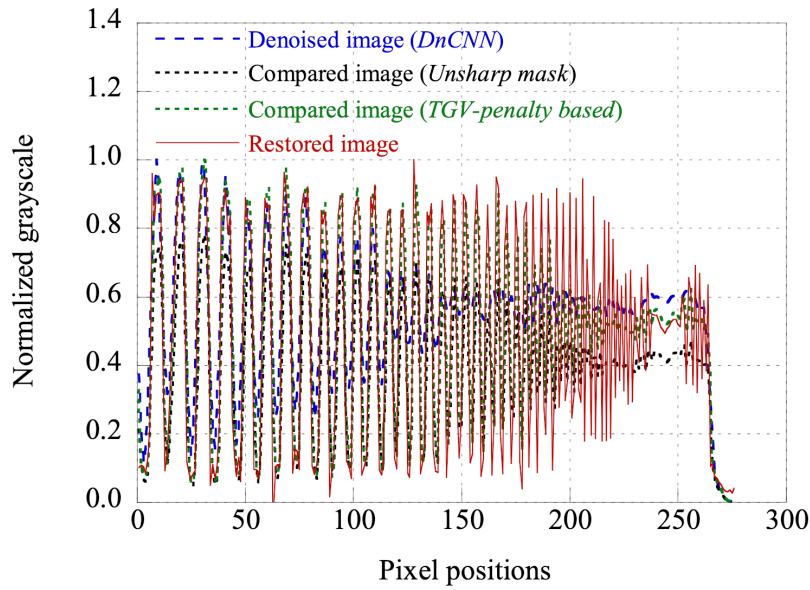


Figure 11. Profiles of line A in figure 10(b).

Acknowledgments

This research was supported by the National Research Foundation of Korea (NRF) grant funded by the Korea government (MSIP) (No. NRF-2017R1C1B2011257).

References

- [1] G. Wang and T.W. Liao, *Automatic identification of different types of welding defects in radiographic images*, *NDT E Int.* **35** (2002) 519.
- [2] M.R. Jolly et al., *Review of non-destructive testing (NDT) techniques and their applicability to thick walled composites*, *Procedia CIRP* **38** (2015) 129.
- [3] D. Mery and D. Filbert, *A fast non-iterative algorithm for the removal of blur caused by uniform linear motion in X-ray images*, in *Proceedings of 15th world conference on nondestructive testing*, Rome Italy (2000).
- [4] A. Buades, B. Coll and J.M. Morel, *A review of image denoising algorithm, with a new one*, *Multisc. Model Simul.* **4** (2006) 490.
- [5] Q. Yang et al., *Low dose CT image denoising using a generative adversarial network with wasserstein distance and perceptual loss*, [arXiv:1708.00961](https://arxiv.org/abs/1708.00961).
- [6] H. Takeda, S. Farsiu and P. Milanfar, *Deblurring using regularized locally adaptive kernel regression*, *IEEE Trans. Image Process.* **17** (2008) 550.
- [7] H. Xu, T. Huang, X. Lv and J. Liu, *The implementation of LSMR in image deblurring*, *Appl. Math. Inf. Sci.* **8** (2014) 3041.
- [8] F. Conte, A. Germani and G. Iannello, *A Kalman filter approach for denoising and deblurring 3D microscopy images*, *IEEE Trans. Image Process.* **22** (2013) 5306.

- [9] M. Figueiredo and R. Nowak, *An EM algorithm for wavelet-based image restoration*, *IEEE Trans. Image Process.* **12** (2003) 906.
- [10] S. Ma, W. Yin, Y. Zhang and A. Chakraborty, *An efficient algorithm for compressed MR imaging using total variation and wavelets*, in *Proceedings of the IEEE Conference on Computer Vision and Pattern Recognition*, Alaska U.S.A. (2008).
- [11] H. Lee, J. Yoon and E. Lee, *Anisotropic Total Variation Denoising Technique for Low-Dose Cone-Beam Computed Tomography Imaging*, *Prog. Med. Phys.* **29** (2018) 150.
- [12] H. Lu, J. Wei, Q. Liu, Y. Wang and X. Deng, *A Dictionary Learning Method with Total Generalized Variation for MRI Reconstruction*, *Int. J. Biomed. Imag.* **2016** (2016) 7512471.
- [13] M.V. Afonso, J.M. Bioucas-Dias and M.A.T. Figueiredo, *Fast Image Recovery Using Variable Splitting and Constrained Optimization*, *IEEE Trans. Image Process.* **19** (2010) 2345.
- [14] R. Gonzalez and R. Woods, *Digital Image Processing*, third edition, Pearson Education, New Delhi India (2009).
- [15] K. Kim et al., *Industrial x-ray inspection system with improved image characterization using blind deblurring based on compressed-sensing scheme*, *Instrum. Sci. Technol.* **45** (2017) 248.
- [16] J. Xie, L. Xu and E. Chen, *Image denoising and inpainting with deep neural networks*, in *Advances in Neural Information Processing Systems*, MIT Press, Cambridge U.S.A. (2012), pg. 341.
- [17] K. Zhang, W. Zuo, Y. Chen, D. Meng and L. Zhang, *Beyond a Gaussian Denoiser: Residual Learning of Deep CNN for Image Denoising*, *IEEE Trans. Image Process.* **26** (2017) 3142.
- [18] H. Fujita et al., *A simple method for determining the modulation transfer function in digital radiography*, *IEEE Trans. Med. Imag.* **11** (1992) 34.
- [19] G.D. Boreman, *Modulation transfer function in optical and electro-optical systems*, SPIE Press, Bellingham U.S.A. (2001).
- [20] F. Sattar, L. Floreby, G. Salomonsson and B. Lovstrom, *Image enhancement based on a nonlinear multiscale method*, *IEEE Trans. Image Process.* **6** (1997) 888.